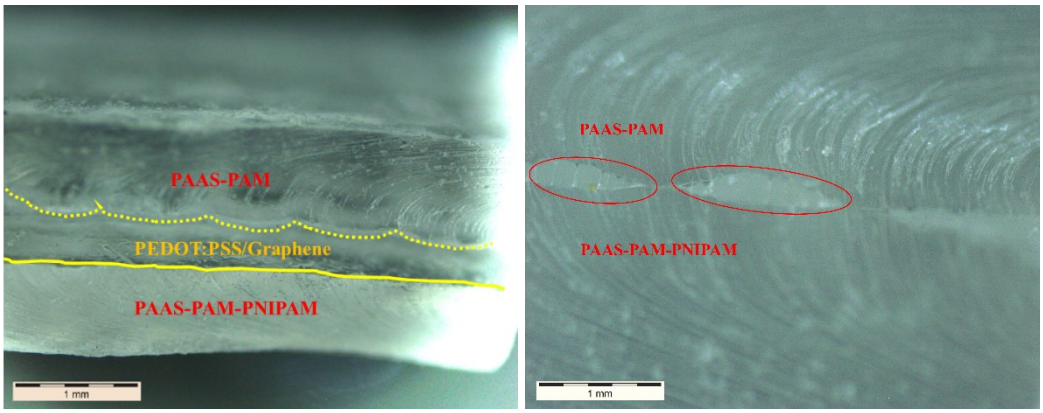

Fig.S1 Fluorescence microscopy for optical imaging of the sandwich-architecture hydrogel.

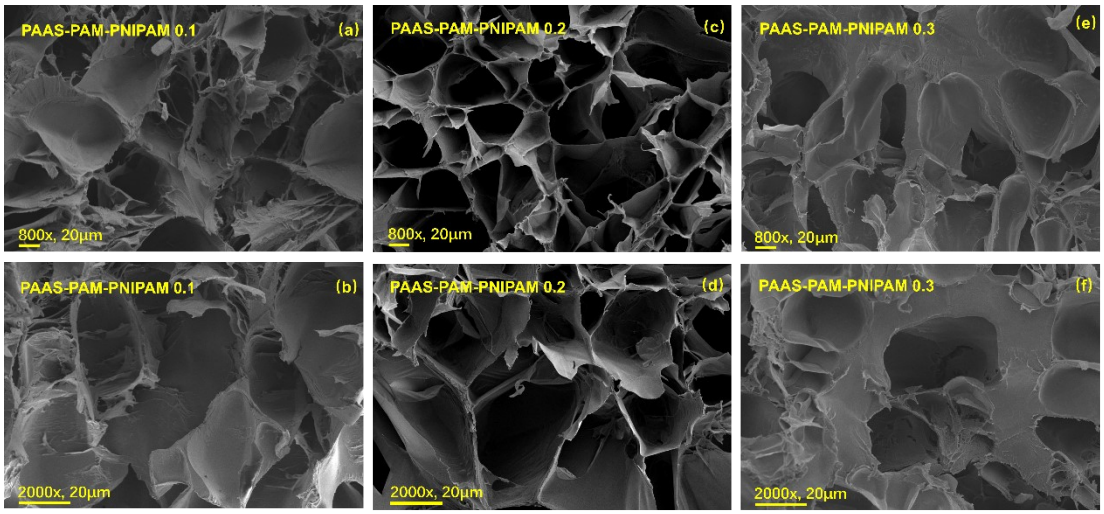

Figure S2. Internal hydrogel network structures of hydrogels corresponding to three different PNIPAM concentrations

The Fourier-transform infrared spectrum of the PAAS hydrogel exhibited a characteristic peak at 1712.63 cm^{-1}, attributable to the asymmetric stretching vibration of the carboxyl group. This peak was absent in the PAAS-PAM hydrogel. The observed absence can be attributed to the following factors: (1) the formation of hydrogen bonds between the amide groups of PAM and the carboxylic acid groups of PAAS, potentially suppressing the vibrational mode of the C=O bond or inducing a shift in its peak position; (2) spectral overlap between the amide I band of PAM (C=O stretching vibration) and certain characteristic peaks of PAAS.

Furthermore, characteristic peaks at 1635.54 cm^{-1} and 1458.08 cm^{-1} were observed, corresponding to the asymmetric stretching vibrations and absorption of the -NH-CO- moiety of the amide groups. The enhanced vibrational activity of the amide groups, promoted by the hydrogen bonding and other interactions between PAAS and PAM, resulted in a significantly lower peak intensity at these positions in PAAS compared to PAAS-PAM. The incorporation of PAM therefore facilitated the interaction within the hydrogel network, thereby enhancing the mechanical strength of the composite.

Upon the introduction of PNIPAM, the PAAS-PAM-PNIPAM hydrogel exhibited a shift in the C-H stretching vibration from 2985.63 cm^{-1} to 3001.21 cm^{-1} relative to PAAS-PAM. This shift suggests the formation of hydrogen bonds between the N-H groups of PNIPAM and either the carboxylic acid groups or other polar moieties within the PAAS-PAM matrix. The formation of such hydrogen bonds directly alters the chemical environment surrounding the C-H bonds, resulting in the observed wavenumber shift of the C-H stretching vibration.

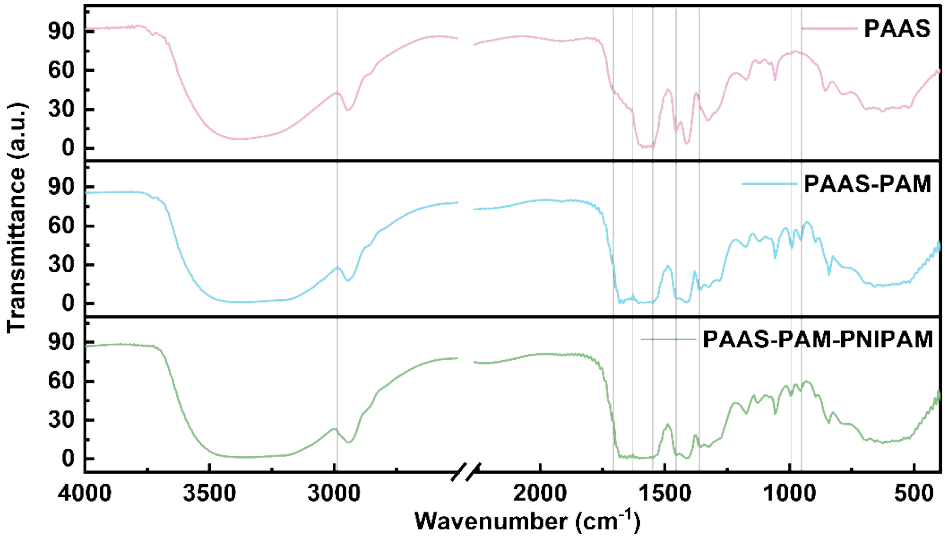

Figure S3. Fourier-transform infrared (FT-IR) spectra of three distinct hydrogels

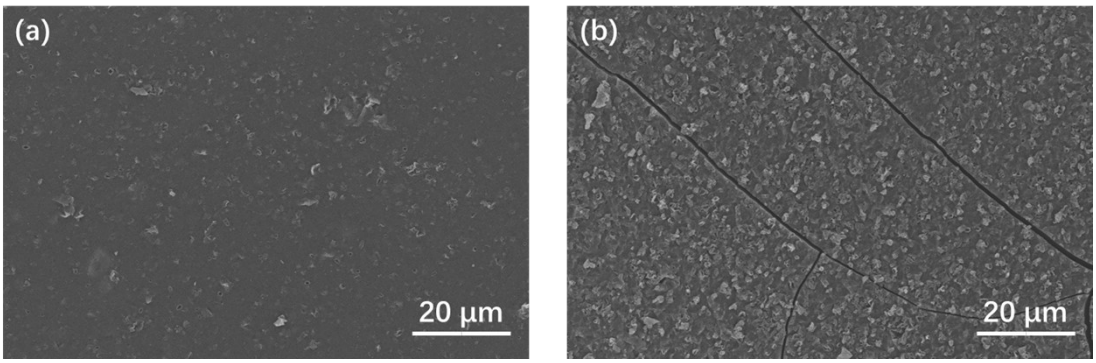

Figure S4. The comparative SEM analysis of the surface topography was conducted (a) pre-tensile and (b) post-tensile deformation.

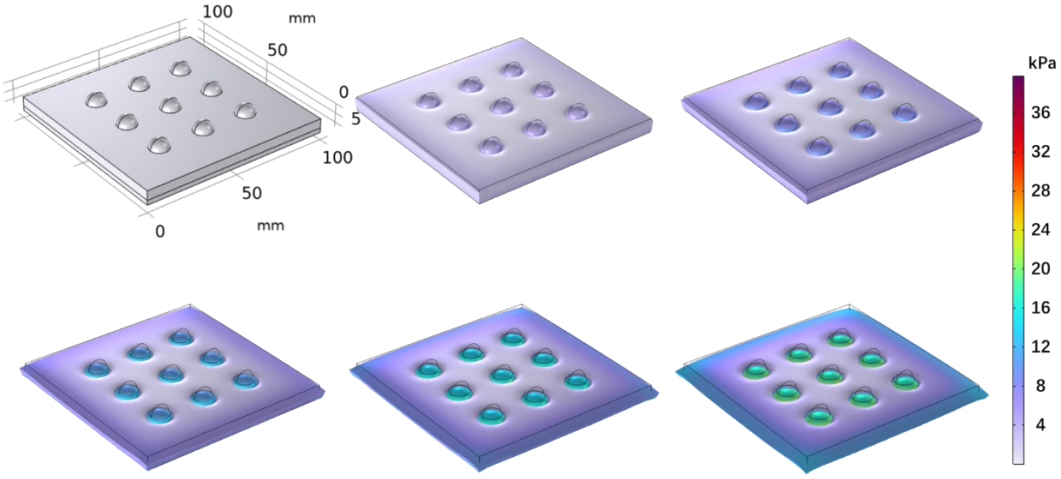

Figure S5. The force distribution across the protruding array as determined by computational simulation.

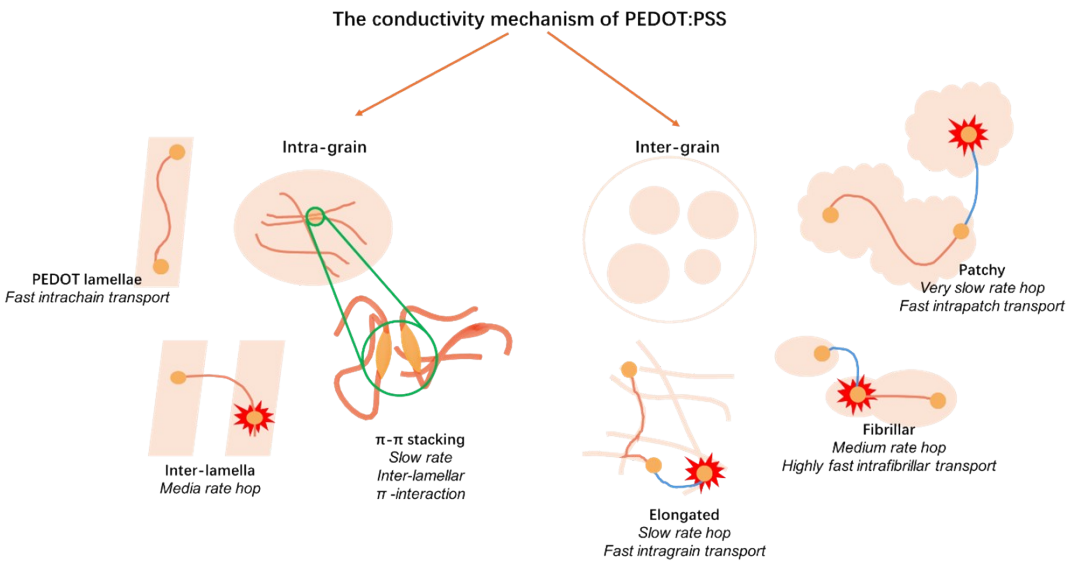

Figure S6. Schematic diagram of PEDOT:PSS polymer conductivity mechanism

As illustrated in Figure S6, the conductivity of PEDOT:PSS stems from an intrinsic mechanism. Electrostatic interactions between cationic PEDOT and anionic PSS monomers facilitate the ordered arrangement of PEDOT oligomers along high molecular weight PSS chains [1, 2]. The entanglement of PSS chains and the π-π stacking interactions between the thiophene rings of PEDOT synergistically drive the formation of colloidal PEDOT:PSS nanoparticles. In aqueous environments, these gel particles exhibit a typical micellar structure, characterized by a hydrophobic core primarily composed of PEDOT and a hydrophilic shell enriched with PSS [3]. When the PSS content in the PEDOT solution is low, PEDOT:PSS crystallites can establish a continuous conductive network, thereby exhibiting high conductivity. However, as the PSS content increases, the conductive network becomes progressively fragmented by PSS regions. Upon exceeding a critical threshold of PSS content, the number of conductive pathways is significantly reduced, leading to a sharp decline in conductivity, and the conductive behavior shifts towards ionic conduction rather than electronic conduction.

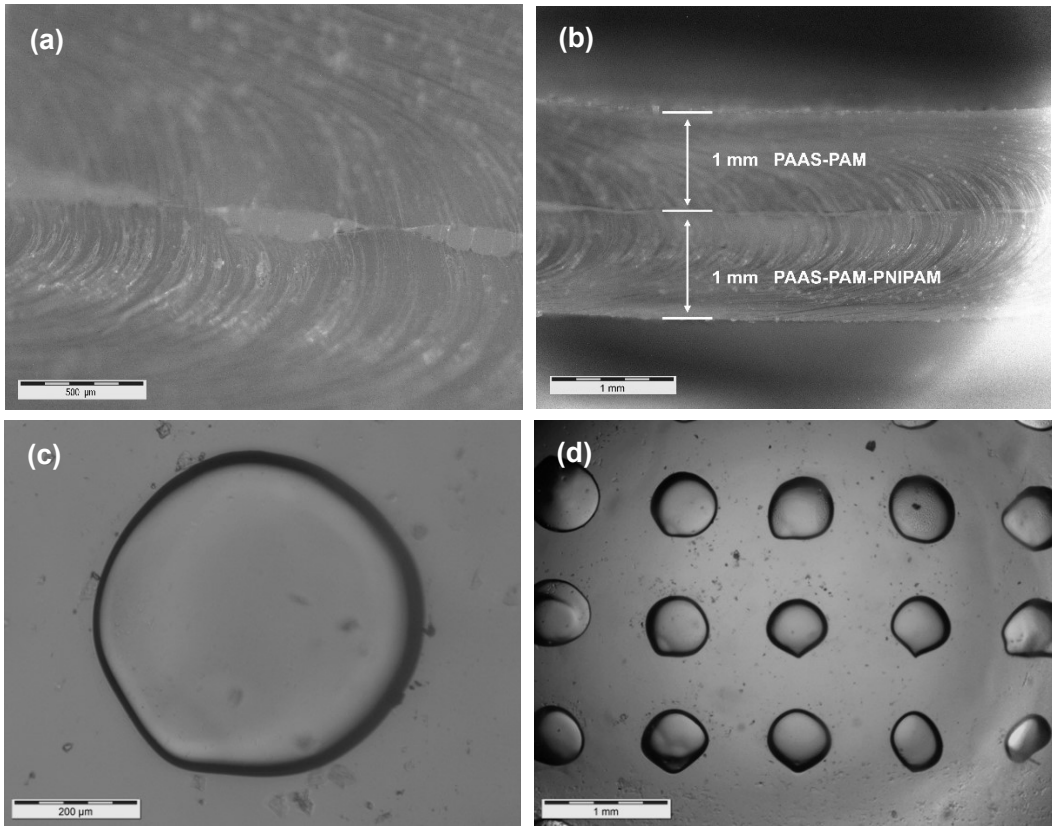

Fig.S7 Fluorescence microscopy for optical imaging of microstructural PAAS-PAM and PAAS-PAM-PNIPAM cross-sections. (a) Optical images of the vertical cross-section at the interface between two gel sheets. (b,e) The thickness of the hydrogel film layers (excluding and including the conductive coating of PEDOT:PSS/Graphene).

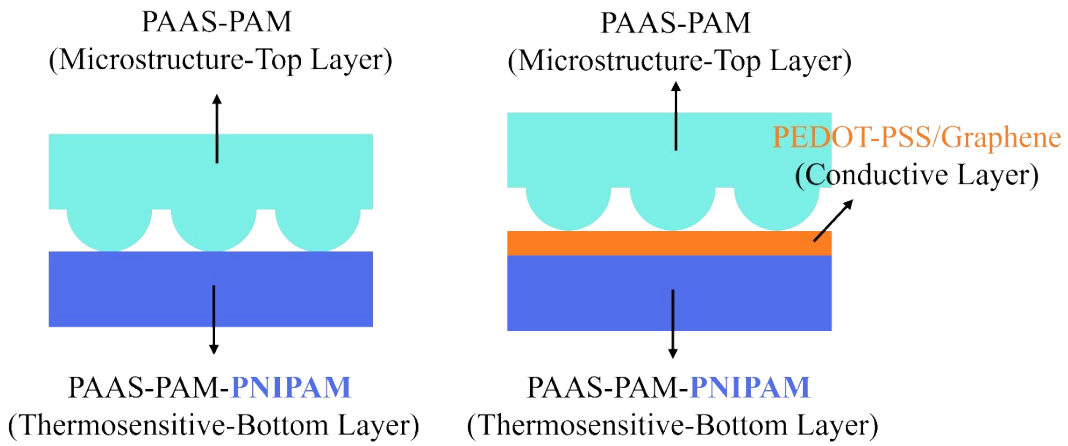

Fig.S8 The appearance, cross-sectional morphology and annotated key dimensions of each layer

Table S1 Comparison of strain and gf performance parameters of existing flexible sensors

and those obtained in this study

Sensor Material System	Structure Type	Conductive Mechanism	Gauge Factor	Strain Range	References
AM-LMA-AMPS-LiCl	Interconnected Network	Ion Conduction	22.15	0-1000%	[4]
3D Print PEDOT:PSS/PVA	Stratified Deposit	Electronic Conductivity	12.78	0-300%	[5]
SCMC/PANI/AC-Bt	Double Network	Electron/Ion Hybrid	12.68	0-1675%	[6]
MXene/PAA	Single Network Combined	Electrical Conductivity	3.64	10-700%	[7]
PVA-HEDP	Homogeneous Composite	Ion Conduction	2.72	0-100%	[8]
Alginate/GO/PAM	Nano Composite	Electron/Ion Hybrid	4.2	0.02-2000%	[9]
rGo-Organohydrogel	Surface Coating	Surface Microcracks	140	0-400%	[10]
PAAS-PAM-PNIPAM/PEDOT:PSS/ Graphene	**Sandwich Structure**	**Electronic Conductivity**	**25.76**	**0-350%+**	**This Work**

Table S2 Comparison of temperature detecting range and TCR performance parameters of existing flexible sensors and those obtained in this study

Sensor materials	Sensing Mechanism	TCR (%/°C)	Test Operating Range (°C)	References
CPVA-QA Elastomer	Improved Ion Mobility	10.8	-	[4]
Carbon Black/Acrylate	Network Thermal Expansion	6.2	33-40	[11]
MXene/PAA	Photothermal/Ionic Effect	-5.27	0-80	[7]
PI/$MnCo_2O_4$	Oxide Semiconductor Ntc	-4.1	-	[12]
Alginate/GO/PAM	Electronic Transition/Ion Migration	2.0-2.7	25-65	[9]
PAAS-PAM-PNIPAM/PEDOT:PSS/ Graphene	**Phase-Change Induced Volume Contraction**	**8.33/16.96**	**30-45**	**This Work**

Table S3 The chemical parameters for each layer of the sandwich structure

Layer	Composition		Sample Name	Concentration	Thickness
Top	**PAAS-PAM**	**Acrylic Acid (AA)**	**PAAS**	**10.5 mol/L**	**1 mm**
		Acrylamide (AM)	**PAAS-PAM**	**0.47 g/mL**	
Mid	**PEDOT-PSS/Graphene**	**PEDOT-PSS /Graphene**	**PEDOT-PSS 0.36~1.44 wt%**	**0.36 wt%**	**300 μm**
				0.72 wt%	
				1.08 wt%	
				1.44 wt%	
			Graphene	**PPS:Gr=1:1 (weight rate)**	

Bottom	**PAAS-PAM-PNIPAM**	**Acrylic Acid (AA)**	**PAAS-PAM-PNIPAM 0.1**	**PAAS**	**10.5 mol/L**	**1 mm**
				PAM	**0.47 g/mL**	
				PNIPAM	**0.1 g**	
		Acrylamide (AM)	**PAAS-PAM-PNIPAM 0.2**	**PAAS**	**10.5 mol/L**	
				PAM	**0.47 g/mL**	
				PNIPAM	**0.2 g**	
		N-isopropylacrylamide	**PAAS-PAM-PNIPAM 0.3**	**PAAS**	**10.5 mol/L**	
				PAM	**0.47 g/mL**	
				PNIPAM	**0.3 g**	

1. Zhang, X., et al., *PEDOT:PSS: From conductive polymers to sensors.* Nanotechnology and Precision Engineering, 2021. **4**(4).
2. Wang, Z. and R. Liu, *PEDOT:PSS-based electrochromic materials for flexible and stretchable devices.* Materials Today Electronics, 2023. **4**: p. 100036.
3. Hosseini, E., V. Ozhukil Kollath, and K. Karan, *The key mechanism of conductivity in PEDOT:PSS thin films exposed by anomalous conduction behaviour upon solvent-doping and sulfuric acid post-treatment.* Journal of Materials Chemistry C, 2020. **8**(12): p. 3982–3990.
4. Fang, X., et al., *Reversibly Cross-Linked Liquid-Free Ionic Conductive Elastomers for Closed-Loop Recyclable Temperature Sensors with Ultrahigh Sensitivity.* CCS Chemistry, 2025. **7**(8): p. 2336–2347.
5. Lina, W., et al., *All 3D-printed high-sensitivity adaptive hydrogel strain sensor for accurate plant growth monitoring.* Soft Science, 2025. **5**(1): p. 2.
6. Wei, J., et al., *High-performance conductive double-network hydrogel base on sodium carboxymethyl cellulose for multifunctional wearable sensors.* Carbohydrate Polymers, 2025. **350**: p. 122943.
7. Lu, Z., et al., *One-Pot Ultrafast Fabricating of MXene-Based Conductive Hydrogel for Dual Strain-Temperature Sensors with Wide Temperature Tolerance.* ACS Applied Polymer Materials, 2025. **7**(15): p. 9933–9946.
8. Shen, B., et al., *An Ultra-Stretchable Sensitive Hydrogel Sensor for Human Motion and Pulse Monitoring.* Micromachines (Basel), 2021. **12**(7).
9. Hou, W., et al., *High performance dual strain-temperature sensor based on alginate nanofibril/graphene oxide/polyacrylamide nanocomposite hydrogel.* Composites Communications, 2021. **27**: p. 100837.
10. Wang, X., et al., *Multifunctional Flexible Sensors Based on rGO@MXene/PDMS Conductive Composites for Human Health Monitoring and Thermal Therapy.* ACS Applied Electronic Materials, 2025.
11. Kwon, H.J., et al., *Carbon black-containing self-healing adhesive hydrogels for endoscopic tattooing.* Sci Rep, 2023. **13**(1): p. 1880.
12. Yan, X., et al., *Water-Soluble GeO2-Transferred Ultrathin PI/MnCo2O4/Ta2O5 Heterostructures for High-Sensitivity Flexible Temperature Sensors with Extreme Stability.* ACS Applied Materials & Interfaces, 2025. **17**(49): p. 67082–67091.